AGU PUBLICATIONS

JGR

Journal of Geophysical Research: Solid Earth

RESEARCH ARTICLE
10.1002/2017JB015077

Key Points:
- The 2016 Tottori earthquake occurred in an intraplate region of Japan
- Deep aftershocks form sharp subparallel lineations, while shallow aftershocks are diffuse and exhibit branching and segmentation
- The 93% of the seismic moment is below 8 km depth, and the radiation efficiency is only 5–7%

Supporting Information:
- Supporting Information S1
- Data Set S1
- Data Set S2

Correspondence to:
Z. E. Ross,
zross@gps.caltech.edu

Citation:
Ross, Z. E., Kanamori, H., Hauksson, E., & Aso, N. (2018). Dissipative intraplate faulting During the 2016 M_w 6.2 Tottori, Japan earthquake. *Journal of Geophysical Research: Solid Earth*, *123*, 1631–1642. https://doi.org/10.1002/2017JB015077

Received 6 OCT 2017
Accepted 19 JAN 2018
Accepted article online 24 JAN 2018
Published online 17 FEB 2018

Dissipative Intraplate Faulting During the 2016 M_w 6.2 Tottori, Japan Earthquake

Zachary E. Ross[1], Hiroo Kanamori[1], Egill Hauksson[1], and Naofumi Aso[2]

[1]Seismological Laboratory, California Institute of Technology, Pasadena, CA, USA, [2]Department of Earth and Planetary Science, University of Tokyo, Tokyo, Japan

Abstract The 2016 M_w 6.2 Tottori earthquake occurred on 21 October 2016 and produced thousands of aftershocks. Here we analyze high-resolution-relocated seismicity together with source properties of the mainshock to better understand the rupture process and energy budget. We use a matched-filter algorithm to detect and precisely locate >10,000 previously unidentified aftershocks, which delineate a network of sharp subparallel lineations exhibiting significant branching and segmentation. Seismicity below 8 km depth forms highly localized fault structures subparallel to the mainshock strike. Shallow seismicity near the main rupture plane forms more diffuse clusters and lineations that often are at a high angle (in map view) to the mainshock strike. An empirical Green's function technique is used to derive apparent source time functions for the mainshock, which show a large amplitude pulse 2–4 s long. We invert the apparent source time functions for a slip distribution and observe a ~16 km^2 patch with average slip ~3.2 m. 93% of the seismic moment is below 8 km depth, which is approximately the depth below which the seismicity becomes very localized. These observations suggest that the mainshock rupture area was entirely within the lower half of the seismogenic zone. The radiated seismic energy is estimated to be 5.7×10^{13} J, while the static stress drop is estimated to be 18–27 MPa. These values yield a radiation efficiency of 5–7%, which indicates that the Tottori mainshock was extremely dissipative. We conclude that this inefficiency in energy radiation is likely a product of the immature intraplate environment and the underlying geometric complexity.

1. Introduction

On 21 October 2016, a M_w 6.2 earthquake (M_{JMA} 6.6) occurred in the Tottori Prefecture of Japan (Figure 1). This left-lateral strike-slip event produced strong ground shaking in the surrounding region, with the largest recorded peak ground acceleration being 1.4 g (Kagawa et al., 2017). The mainshock was preceded by 70 foreshocks over a 12 h period, including one with M 4.2. The Japanese Meteorological Agency (JMA) detected 9,639 earthquakes over the course of this sequence between 21 October 2016 to 31 October 2016, which are shown in Figure 1. The aftershocks are notably diffuse in character without a well-defined fault plane visible from the JMA locations; they are however concentrated in two main clusters.

In Southwest Japan, oblique subduction of the Philippine Sea Plate drives thrust events at the plate interface, while in the intraplate regions of Shikoku and Chugoku, strike-slip events result from slip partitioning (Figure S3). While the Median Tectonic Line in the Shikoku region is a mature strike-slip fault, recent GPS observations revealed shear localization in the San-in Shear Zone in the Chugoku region (Nishimura & Takada, 2017). The San-in Shear Zone, within the larger Northern Chugoku Shear Zone (Gutscher & Lallemand, 1999), has a history of diverse earthquake activity including swarms (Shibutani et al., 2002), deep low-frequency earthquakes (Aso & Ide, 2014; Aso et al., 2013; Ohmi & Obara, 2002), and several moderate to large earthquakes in the last century (Kanamori, 1972; Nishida, 1990; Pulido & Kubo, 2004; Shibutani et al., 2002), despite the low rate of strain accumulation (Nishimura & Takada, 2017). In 1943, the M_w 7.0 Tottori earthquake occurred east of the 2016 hypocenter (yellow line, Figure 1) and ruptured the Shikano and Yoshioka faults (Kaneda & Okada, 2002; Omote, 1943; Tsuya, 1944). In 2000, the M_w 6.7 Western Tottori earthquake occurred approximately 50 km to west of the 2016 Tottori earthquake (Figure 1). The relocated aftershocks in this sequence form a network of complex lineations with a (generally) northwest trend, and many of these lineations branch out from the main rupture plane at subparallel angles (Fukuyama et al., 2003).

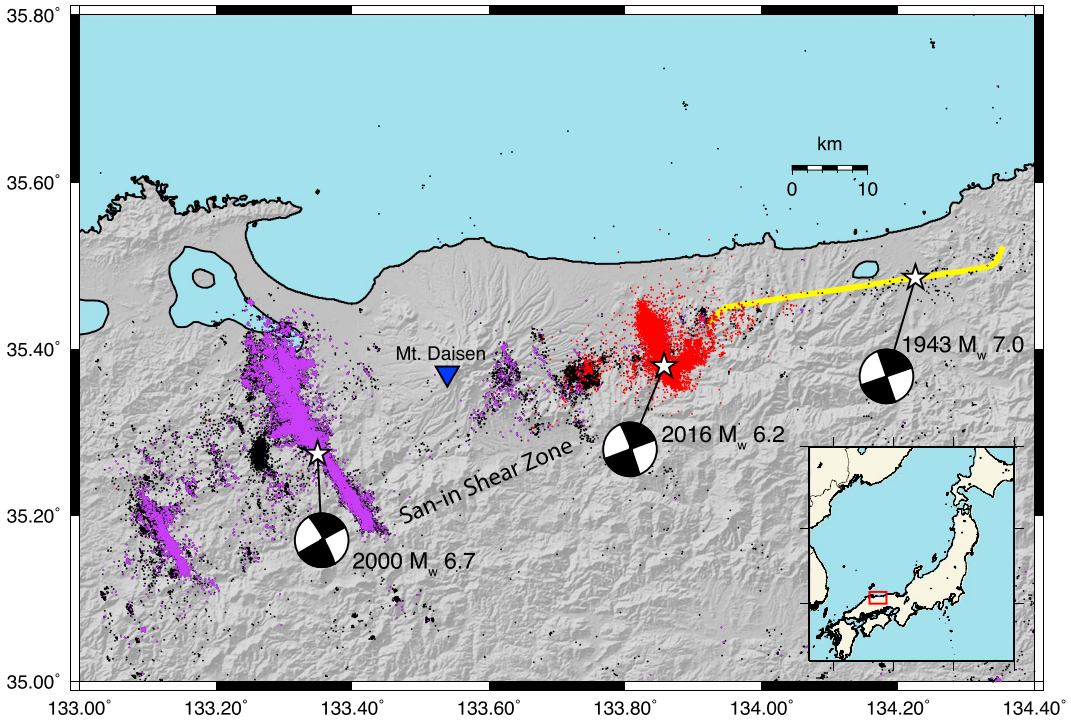

Figure 1. Map of Tottori, Japan region. Seismicity from JMA unified catalog shown as black dots, with the 2000 and 2016 Tottori sequences shown in purple and red, respectively. Hypocenters of the 1943, 2000, and 2016 earthquakes are indicated by white stars. Rupture plane of the 1943 earthquake is shown in yellow (Kanamori, 1972). A significant amount of seismicity was triggered far away from the 2000 and 2016 ruptures.

The relationship between the earthquake source process and the internal structure of fault zones is an active subject of research. For example, dynamic generation of brittle damage within fault zones (Li et al., 2006) may affect the rupture process and seismic energy (Xu et al., 2015). Such processes have the potential for enhanced nondouble couple source terms (Ben-Zion & Ampuero, 2009). Fault roughness and the degree of localization of the primary slip surface may affect the seismic efficiency and rupture velocity (Shipton et al., 2006; Wilson et al., 2005). Ruptures on bimaterial faults may propagate more favorably in the direction of motion of the more compliant medium (Andrews & Ben-Zion, 1997; Weertman, 1980). However, the relationship between the rupture process of individual earthquakes and their host fault zone structure is generally difficult to establish.

In this study, we derive high-resolution earthquake hypocenters using a matched-filter algorithm for tens of thousands of earthquakes in the 2016 Tottori sequence. An empirical Green's function method is used to provide a detailed view of the rupture process and energy budget for the 2016 Tottori mainshock. Together, the seismicity and source properties of the mainshock suggest that this intraplate earthquake was highly inefficient in energy radiation, which may be a product of the geometrical complexity of the underlying immature fault structures.

2. Data

We use data from four seismic networks provided by the National Research Institute for Earth Science and Disaster Prevention of Japan. Continuous short-period data (21 October 2016 to 31 October 2016) from Hi-net are used at 88 stations located generally within 100 km of the mainshock hypocenter (Figure 2). These data are decimated to 50 Hz and band-pass filtered between 2 and 15 Hz. We also use the K-NET and KiK-net accelerograms for the M_w 6.2 mainshock and a M 4.2 foreshock (2016/10/21 12:12:23) at a total of 70 stations (Figure 2). Finally, we use F-net broadband recordings at 68 stations. The initial seismicity catalog of 9,639 events (Figure 1) was produced by JMA.

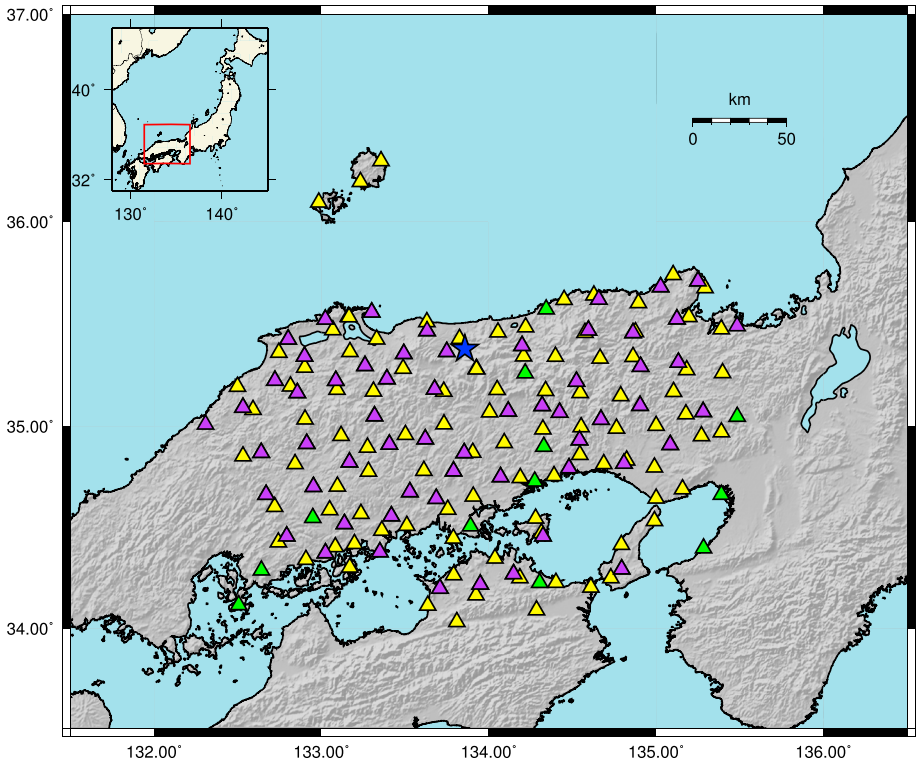

Figure 2. Map of seismic stations used. The networks used are Hi-net (green), K-NET (yellow), and KiK-net (purple). Some sites have multiple sensor types. Blue star indicates hypocenter of mainshock.

3. Methods and Results

3.1. Matched-Filter Earthquake Detection

We use the template matching algorithm of Shelly et al. (2016), along with the modifications of Ross, Rollins, et al. (2017), to detect previously unidentified earthquakes in the continuous data. We use all events in the JMA catalog as template events to search for similar signals. First, an automated picking algorithm is used (Ross et al., 2016) to try and pick *P* and *S* waves for all events at each station. When a pick is unsuccessful, 1-D predicted arrival times are determined from the model of Shibutani et al. (2005). *P* wave templates are constructed from the vertical component only using window lengths up to 2.5 s (depending on the *S-P* time), while *S* wave templates are constructed from both horizontal components using a window length of 4 s. A signal-to-noise ratio is determined for each template waveform using an equivalent length of noise prior to the *P* wave arrival, and if less than 5.0, the template waveform is discarded. A minimum of 12 channels with templates are then required in order to proceed; otherwise, the template event is skipped. Then, for a given event, each template is correlated against 24 h of continuous data. Correlation functions are migrated back in time by an amount equal to the travel time and stacked over all phases and channels. Events are detected using a threshold of 8 times the median absolute deviation for the day (Shelly et al., 2016), which commonly results in thresholds in the range of 0.4–0.8. Applying this procedure results in 45,137 events, which is 4.68 times as many as listed in the JMA catalog.

For each detected event, we then recorrelate it with the 200 nearest template events to measure differential times for relocation purposes (e.g., Hauksson et al., 2012). Here we use shorter window lengths of 1.5 s for both the *P* and *S* waves, with both phases used on all three components. When more than one differential time is measured for a phase at a given station, the channel with the largest cross-correlation coefficient is selected. A minimum of six differential times are required to save a given pair, resulting in 43,999,278 total differential times for all pairs. Then we attempt to relocate all events with the GrowClust algorithm (Trugman & Shearer, 2017), which iteratively groups events into clusters and relocates them with the differential time data. GrowClust was selected because the algorithm has only a few sensitive parameters, and these are relatively simple to tune. For the relocation, a minimum correlation coefficient of 0.75 is used for

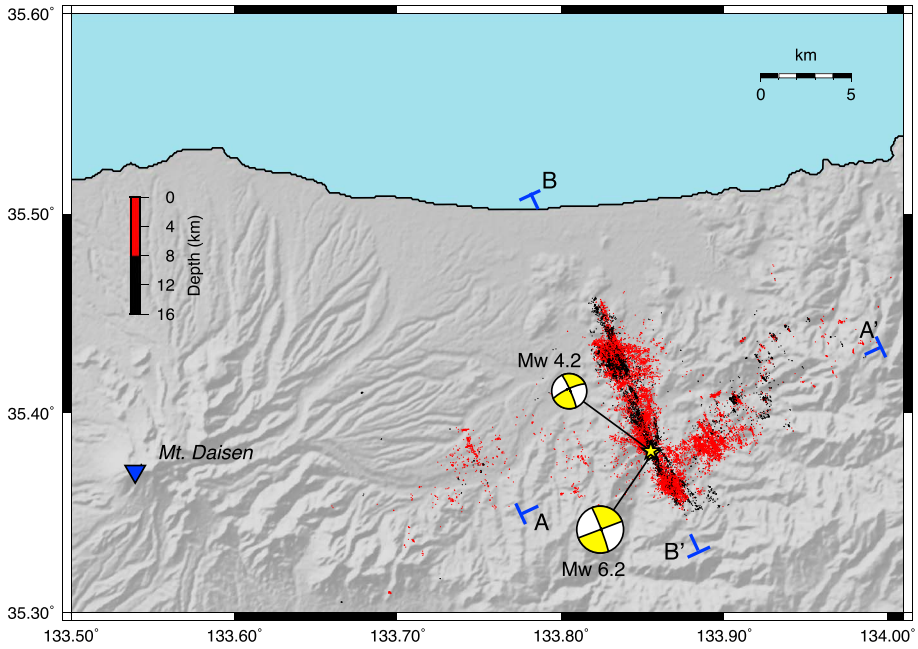

Figure 3. Map of relocated seismicity detected with the matched-filter algorithm. Shallow seismicity (red) is more diffuse, displays more branching and segmentation, and was triggered throughout the region. Deep seismicity (black) is highly localized and less segmented.

determining cluster similarity, and correlation values below 0.6 are discarded. At least six differential times per pair are required as well. A 1-D velocity model for the region is used (Shibutani et al., 2005). A more detailed description of the method is given in Trugman and Shearer (2017). In total, 20,039 events are successfully relocated (44%), which is primarily due to the low signal-to-noise ratios of the newly detected events.

Additionally, we determine moment tensor solutions for the mainshock and M 4.2 foreshock event using the W-phase algorithm (Duputel et al., 2012; Kanamori & Rivera, 2008). For the mainshock, the best fitting strike, dip, and rake are 339.2°, 86.5°, and 0.1° respectively. For the M 4.2 foreshock, the best fitting strike, dip, and rake are 336.2°, 84.5°, and 11.6° respectively. Examples of waveform fits for selected stations are shown in Figures S1 and S2 in the supporting information.

Figure 3 shows the relocated seismicity in map view. The two main clouds that were visible in the JMA hypocenters (Figure 1) now appear as networks of smaller faults. These structures exhibit a high degree of branching but have a dominant trend parallel to the strike of the mainshock (339°). Additionally, numerous structures with a length generally less than 500 m were activated away from the primary seismicity cloud, with some events being as far as 15 km away. These tiny faults also share the same northwestern trend of the mainshock and further the regional trend of seismicity (Figure 1).

Next we examine the seismicity in a fault-normal cross section through the hypocenter (Figure 4a). In this plot, the seismicity is restricted to events that occurred within 3 km of the plane. There is a major near-vertical fault structure visible that contains most of the aftershocks. This structure is about 2 km wide in the upper 8 km and is rather diffuse in character. Nearly all the events below 9 km are within a ~500 m wide zone that extends down to about 15 km. This type of behavior is reminiscent of fault zone flower structures (Ben-Zion & Sammis, 2003) and may reflect the increasing confining pressure with depth. The relatively deep extent of the broader portion of the fault zone may reflect the immaturity of the fault zone. The sizable group of lineations northeast of the hypocenter in Figure 3 is also strongly visible between 2 and 8 km distance along A-A′, and these structures have a general depth extent of about 2 km. We also note that the depth of the top of the seismicity decreases here toward the northeast.

Figure 4b contains a fault-parallel cross section of seismicity within 1 km of the B-B′ plane. Near the hypocenter (blue star) there is a ring of seismicity approximately 10 km long and 4 km deep, which suggests some

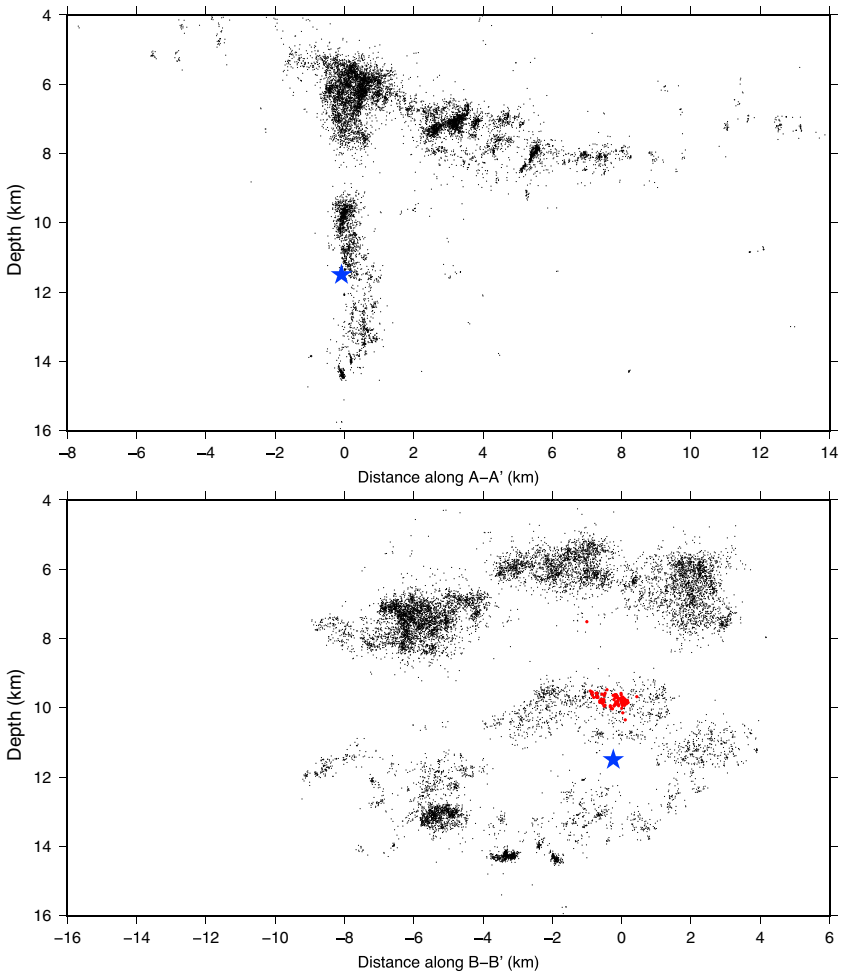

Figure 4. Fault-normal (a) and fault-parallel (b) cross sections of seismicity. Profiles are defined in Figure 3. Mainshock hypocenter is denoted by blue star, and foreshocks are indicated by red dots.

relationship to the mainshock rupture process. There are also three small shallow clouds. With a more complete view of the fault structure in this region, we now proceed to determining earthquake source properties for the Tottori mainshock.

3.2. Finite Fault Inversion

We use an empirical Green's function (EGF) method to derive apparent source time functions (STF) using high-quality accelerograms (Ross, Kanamori, & Hauksson, 2017). Here we use the term apparent source time function to represent the source time function (moment-rate function) as viewed from the station. A smaller M 4.2 foreshock is used as an EGF to deconvolve propagation and site effects (Figure 3). The foreshock and mainshock are located approximately 300 m apart. First, all accelerograms are rotated to the transverse component and windowed starting 0.5 s before the *P* wave arrival and ending 30 s later. The target event and EGF records are low-pass filtered at 0.75 Hz, and the deconvolution is performed with an iterative time-domain deconvolution algorithm (Kikuchi & Kanamori, 1982; Ligorría & Ammon, 1999). Of the 70 STF produced, 38 explained at least 70% of the variability in the target record, and form the subset used in the subsequent analysis (Figure 5).

The STFs have several notable features that are common to all stations. First, a high-amplitude pulse with a duration of roughly 2–4 s is present. The timing of the peak of this pulse varies azimuthally, with the shortest values being in the 340° strike direction, and the longest values being near 160°. These observations are diagnostic of rupture directivity along the direction N20°W. In summary, the southeastern azimuths have STFs that are about 4 s in duration, while the northwestern azimuths have STFs that are 2 s.

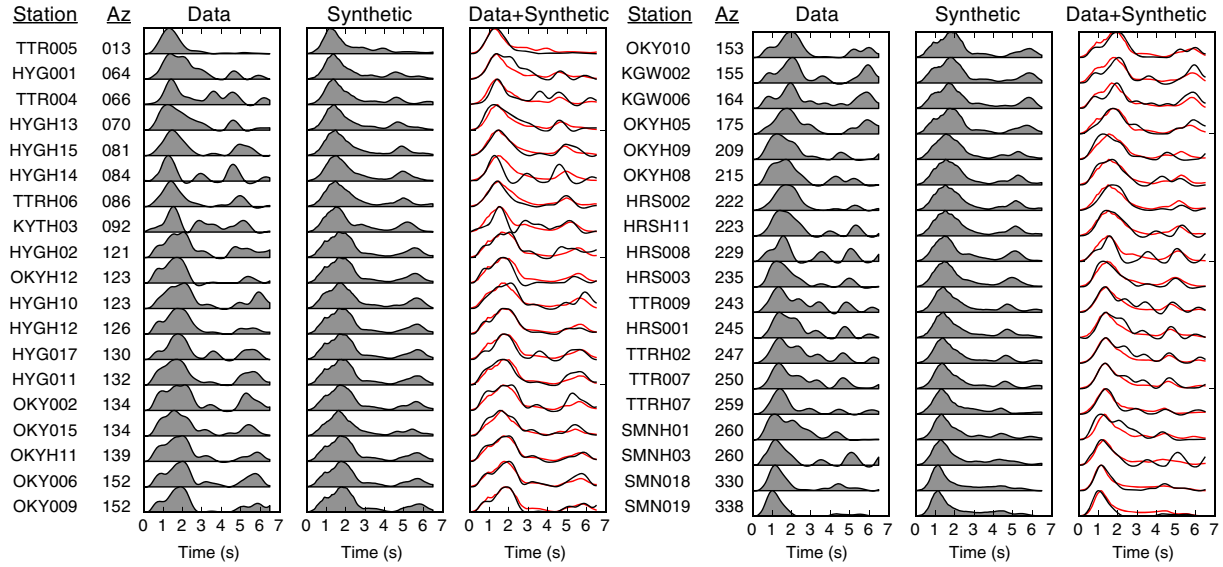

Figure 5. Apparent source time functions for both data and synthetics. Stations are ordered by azimuth and display a dominant pulse 2–4 s in duration with northwest rupture directivity characteristics. A second weak pulse is visible around the 4–6 s mark.

Next we used the STFs in a linear slip inversion, following Ross, Kanamori, & Hauksson, 2017. The onset of each STF was manually picked and set as the origin time. The STFs were truncated at 6.5 s based on the observed duration in the southeastern azimuths and normalized to an area equal to the seismic moment (2.54×10^{18} N m). The fault plane is divided into N_x by N_y subfaults that are numbered from $i = 1$ to N (i.e., $N = N_x N_y$). We set $N_x = 20$, $N_y = 15$, with grid spacing equal to 0.75 km, using the strike and dip of the mainshock focal mechanism. Each subfault is placed at a grid point i. Let v, l_i, t_{ij}, and $M_j(t)$ be the rupture velocity, distance of the ith subfault from the hypocenter on the fault plane, travel time from the ith grid cell to the jth station. Then, the moment-rate function at the jth station is given by

$$M_j(t) = \sum_{i=1}^{N} m_i \left[t - \left(\frac{l_i}{v} + t_{ij} \right) \right]. \quad (1)$$

We determine $m_i(t)$ by minimizing the difference between $M_j(t)$ and the observed moment-rate functions. The t_{ij} values are calculated using the layered 1-D structure of Shibutani et al. (2005). For the inversion, we represent the local moment-rate function as a superposition of K symmetric triangles $s(t)$ with a half-duration t_h and a unit amplitude:

$$m_i(t) = \sum_{k=1}^{K} a_{ik} s(t - (k-1)t_h). \quad (2)$$

This representation allows us to perform a linear inversion to determine the amplitudes a_{ik}. The slip-rate function $d_i(t)$ for the ith subfault is given by $d_i(t) = m_i(t)/\mu_i s$, where μ_i and s are the rigidity at the subfault depth, and the subfault area, respectively. Here we use $K = 5$ and $t_h = 0.5$ s to parameterize the slip rate function (e.g., Hartzell & Heaton, 1983). The amplitudes of these triangles are the only parameters solved for, because the time series used here are apparent source time functions, rather than far-field displacement seismograms. Laplacian regularization was used, with the weighting chosen using the "L-curve" approach (Aster et al., 2012). The synthetic STFs produced from the inversion are shown in Figure 5. It can be seen that the synthetics reproduce all of the main features observed in the data STFs.

Figure 6 shows the slip model (rupture velocity of $0.7v_s$) projected onto vertical profile B-B′ (Figure 3), alongside the relocated seismicity. The maximum slip is 5.3 m, although the exact numerical value depends on the grid size, choice of regularization, and rupture velocity assumed. A large slip patch approximately 4 km in diameter is present and asymmetric about the hypocenter. This feature of the slip model is consistent with the large initial pulse of the STFs in Figure 5. The second pulse visible in the STFs (Figure 5) is much more incoherent across the network than the large initial pulse and results in the slip from this pulse being broadly distributed rather than localized.

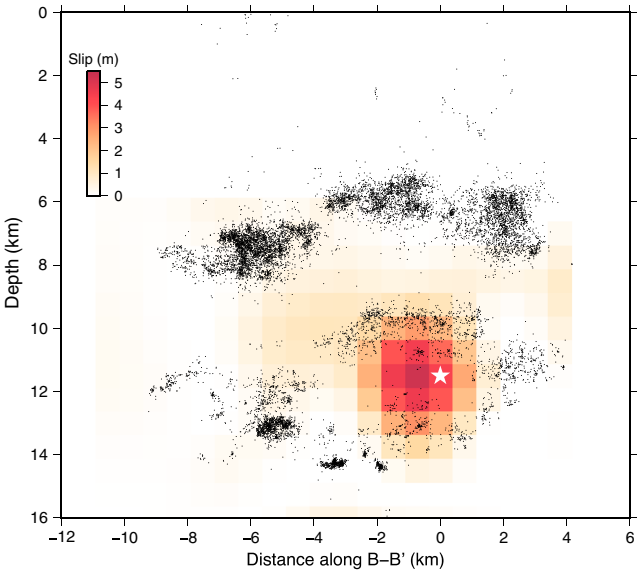

Figure 6. Slip distribution derived from linear inversion of apparent source time functions. B-B′ profile is defined in Figure 3. Hypocenter is indicated by the white star. The rupture propagates predominantly to the northwest, with 93% of the moment occurring below 8 km. Note the ring of seismicity surrounding the large slip patch.

Many investigations (Beroza, 1991; Beroza & Spudich, 1988; Mendoza & Hartzell, 1988) have documented aftershock zones that appear to be anticorrelated with slip. In a high-resolution study of a M_w 5.2 earthquake on the San Jacinto fault in Southern California, Ross, Kanamori, & Hauksson, 2017 found almost complete absence of aftershocks in the main slip zone. For the Tottori earthquake, the large slip patch is also surrounded by a ring of aftershocks.

Varying the rupture velocity and grid size influences the model, but the big slip patch is always in the same location, with nearly constant rupture length of 4–5 km. The down-dip width of the rupture area increases with velocity due to a lack of constraints in this direction. If we assume that the aftershock seismicity bounds the slip patch, then a rupture velocity of about ~0.5–0.6 v_s results in a slip model that is most consistent with the seismicity. Using the difference in pulse widths between the forward and reverse propagation directions in a standard directivity style analysis results in a rupture length of ~4 km and a rupture velocity of 1.89 km/s (see Appendix A). Considering that the seismicity is about a factor of 4 more localized (in the fault-normal direction) below 8 km depth together with the lack of shallow slip in the model, it is likely that the rupture did not extend above 8 km.

Kubo et al. (2017) also derived a slip model for the 2016 Tottori earthquake using the closest strong-motion records and a traditional finite-fault inversion. Their model has a main asperity located generally in the same place as ours but is distributed over an area that is more than 4 times as large. It further is symmetric with respect to the hypocenter, with no evidence of directivity. Their inversion did not include the island stations in the forward direction of the rupture (SMN018 and SMN019), which exhibit a clear narrow pulse ~2 s in duration (Figure 5). These stations help to constrain the directivity of the main slip patch, which in turn provides an important constraint on the rupture length.

3.3. Stress Drop and Energy Calculations

Next, the slip model is used to calculate the static stress drop, using the method of Ye et al. (2016). First, we place our slip model in a homogeneous half-space using the same geometry as the Tottori mainshock and

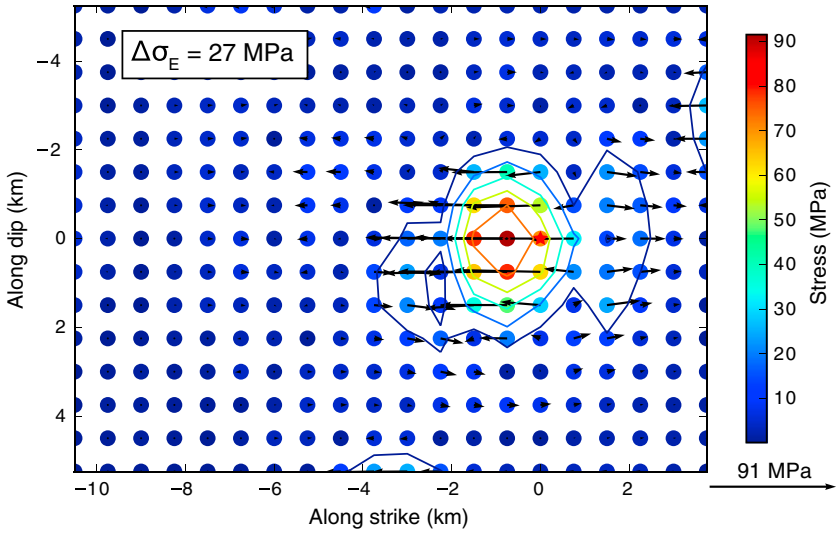

Figure 7. Stress drop distribution on the fault plane determined as a superposition of stress for each subfault. The slip-weighted stress drop is 27 MPa. Vectors indicate the orientation of shear stress at each point.

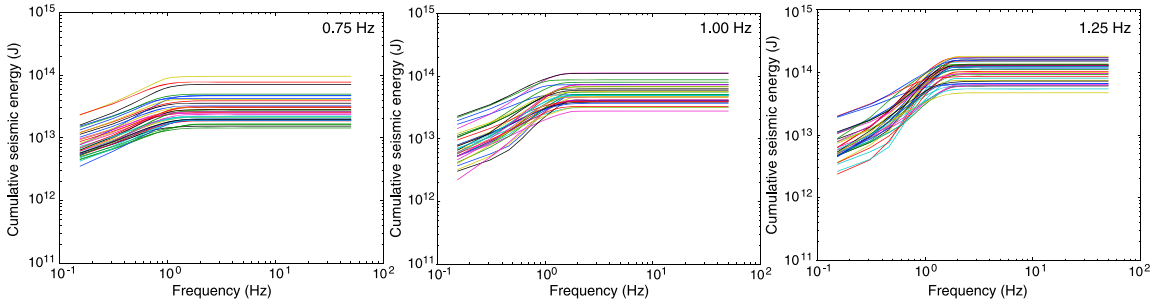

Figure 8. Cumulative energy spectra derived from the source time functions. The frequency values displayed in the upper right corner indicate the cutoff frequency of the low-pass filter applied before deconvolution. Around 1 Hz, the energy spectra become dominated by noise, which artificially increase the estimate of the seismic energy.

determine the stress distribution as a superposition of stress for each subfault computed with the code of Okada (1985), (Figure 7). The average rigidity of our fault model (30 GPa) is used for the rigidity of the half-space. Then we compute a slip-weighted stress drop, $\Delta\sigma_E$,

$$\Delta\sigma_E = \frac{\int_\Sigma \Delta\sigma \Delta u ds}{\int_\Sigma \Delta u ds}, \tag{3}$$

which is directly related to the earthquake strain energy (Noda et al., 2013). Rupture velocities in the range 0.5–0.8v_s (1.8–2.9 km/s) yield 18–27 MPa for the stress drop.

From here, we calculate the seismic energy, E_R from the spectra of the STFs following Ross, Kanamori, & Hauksson, 2017 and Vassiliou and Kanamori (1982).

$$E_R = KM_0^2 I, \tag{4a}$$

$$K = \left[\left(1/15\pi\rho\alpha^5\right) + \left(1/10\pi\rho\beta^5\right)\right], \tag{4b}$$

$$I = 8\pi^2 \int_0^\infty f^2 |S(f)|^2 \, df, \tag{4c}$$

where $S(f)$ denotes the Fourier transform of the source time function, $s(t)$, normalized to unit area, at a given station. The spectra are derived with a multitaper algorithm (Prieto et al., 2009; Thomson, 1982). We calculate equation (4a) for each station using values for α, β, and ρ of 6.2 km/s, 3.6 km/s, and 2,700 kg/m^3, respectively. Equation (4c) is calculated up to 0.75 Hz, which is the frequency of the low-pass filter used in the deconvolution algorithm. The final value is computed by taking the median over all stations. Using an omega-square model (Brune, 1970) with a corner frequency of 0.48 Hz to correct for the missing energy results in $E_R = 4.1 \times 10^{13}$ J.

To further investigate the effect of the low-pass filter and cutoff frequency on the seismic energy, we compare STFs using 0.75 Hz, 1.0 Hz, and 1.25 Hz low-pass filters in the deconvolution process. Figure 8 shows the cumulative spectral energy for each case. The 0.75 Hz and 1.0 Hz cases have spectra that are relatively simple, but for the 1.25 Hz case, the cumulative energy jumps dramatically around 1 Hz. This suggests that noise in the STFs is dominating the integral. This is likely due to these frequency values approaching the corner frequency of the EGF, which we estimate around 1.25–1.5 Hz based on flattening in the spectra of the STFs. Using the cutoff frequency to correct for the missing energy with an omega-square model results in E_R estimates of 5.75×10^{13} J and 1.22×10^{14} J for the 1.0 Hz and 1.25 Hz cases. Choosing a low cutoff frequency reduces the noise in STF and allows an accurate estimation of E_R up to the cutoff frequency. However, a large correction for the missing energy above the cutoff frequency must be added. In contrast, choosing a higher cutoff frequency reduces the correction for the missing energy, but the noise in STF leads to an overestimate of E_R. We choose a cutoff frequency of 1 Hz as a compromise. Then, the moment-scaled energy is determined to be $\varepsilon = E_R/M_0 = 2.3 \times 10^{-5}$.

As the seismic energy and stress drop were independently calculated, we can use these to calculate the radiation efficiency (Kanamori & Rivera, 2006)

$$\eta_R = \frac{E_R}{\Delta W_0} = \frac{2\mu}{\Delta\sigma_E}\left(\frac{E_R}{M_0}\right). \tag{5}$$

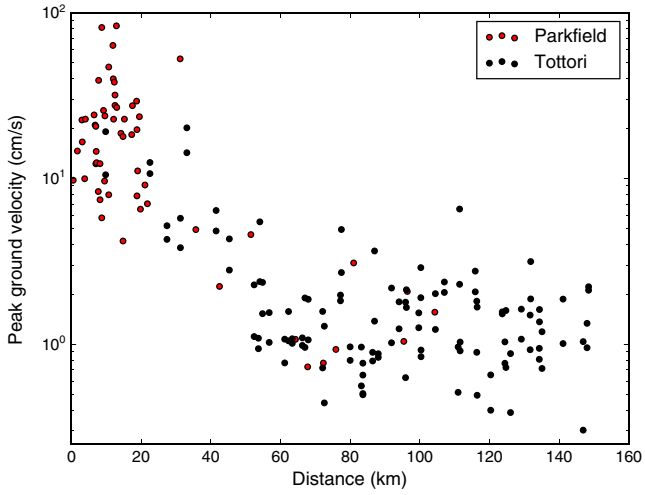

Figure 9. Comparison of peak ground velocity for the 2004 M_w 6.0 Parkfield and 2016 M_w 6.2 Tottori earthquakes. Both earthquakes display similar peak ground velocity over the entire distance range, suggesting that the radiated seismic energy is similar for both earthquakes. This is in contrast to the large difference in stress drop.

Here, $\Delta W_0 = \Delta\sigma_E M_0/2\mu$ is the available strain energy. Applying equation (5) with the range of stress drops obtained previously results in η_R = 5.1 – 7.7 % . This indicates that about 92–95% of the available strain energy went into thermal and fracturing processes near the rupture tip and off-fault. We note that the radiation efficiency is not the same as the seismic efficiency, which also includes the energy dissipation due to sliding friction.

3.4. Comparison With the 2004 Parkfield Earthquake

To give additional context to the discussed results, we now compare the 2016 Tottori earthquake with the 2004 M_w 6.0 Parkfield earthquake. We use accelerograms of the Parkfield earthquake recorded by 58 stations of the California Geological Survey and United States National Strong-Motion networks. Figure 9 contains a plot of peak ground velocity (PGV) as a function of distance for both the Parkfield and Tottori earthquakes. Here we use PGV as a proxy for seismic energy. It can be seen that, in general, PGV for both earthquakes is within the observed scatter over the full distance range. This suggests that the seismic energy for these events is similar. However, the rupture area for the Parkfield earthquake is considerably larger (Kim & Dreger, 2008), as is the length of the aftershock zone. Estimates of the static stress drop for the Parkfield earthquake are in the range of ~2 MPa (Allmann & Shearer, 2007; Kim & Dreger, 2008), which is about an order of magnitude less than the stress drop estimated for the Tottori earthquake. Thus, while the seismic energy appears to be rather similar between the two events, the large discrepancy in stress drop implies that the Parkfield earthquake was 8–14 times as efficient in energy radiation as the Tottori earthquake.

4. Discussion

The 2016 M_w 6.2 Tottori earthquake bears several similarities to the previous 1943 M_w 7.0 and 2000 M_w 6.7 Tottori earthquakes, and also some significant differences. The 2000 and 2016 events had left-lateral strike-slip motion on northwest-southeast trending faults, while the 1943 event had right-lateral strike-slip motion on an east-west trending fault (Kanamori, 1972). The 1943 event produced some surface rupture (Kaneda & Okada, 2002; Tsuya, 1944), while the 2000 (Semmane et al., 2005) and 2016 events had no reported surface rupture. From the model in our study, the 2016 event ruptured predominantly in a horizontal direction, extending from a depth of 11.5 km up to a depth of about 8 km. In contrast, the 2000 earthquake nucleated at about 14 km and primarily ruptured upward, with most of the slip being shallow (Semmane et al., 2005). The 1943 Tottori earthquake ruptured both the Yoshioka and Shikano faults, which are separated by about 2 km on the surface (Kaneda & Okada, 2002; Tsuya, 1944). The relocated seismicity for the 2016 sequence displays similar geometric complexity to the 2000 sequence (Fukuyama et al., 2003), and both sequences have most of the aftershocks forming networks of well-defined lineations with a high degree of segmentation and branching.

Both the 2000 and 2016 earthquakes triggered significant off-fault seismicity as much as 15–20 km from the primary fault plane (e.g., Fukuyama et al., 2003). While earthquake triggering is commonly observed in fault zones around the world, the spatial extent of triggering observed in the Tottori region appears to be unusually extensive; this may indicate that a property of the fault structure is making the region more susceptible to triggering. Although the mainshock rupture area at depth is relatively localized, this may be more related to the internal fault structure and the increased confining pressure at depth.

The spatial distribution of seismicity has an unusual pattern, in that the deeper events are very localized and composed of sharp, subparallel lineations, while the shallow events are rather diffuse and out of plane of the mainshock rupture. Our slip model indicates that the mainshock had about 93% of the seismic moment below 8 km (Figure 6). These two observations seem to suggest that the deeper seismicity is on the primary rupture plane, while the shallower events may be mostly or entirely off-fault. As the 2000 and 2016 ruptures never reached the surface, and only a fraction of the total rupture length for the 1943 earthquake produced

surface rupture, the rupture behavior in the shallow material may have been controlled by the fault structure during these events. Indeed, the San-in Shear Zone is notable for having no active faults identifiable on the surface, despite the history of earthquake activity (Nishimura & Takada, 2017). Thus, for these faults a single localized interface may not extend all the way to the surface; at shallow depths, the fault zone may form distributed zones of damaged rock instead. As the fault zone matures, the shallow structure may localize further (Ben-Zion & Sammis, 2003). These factors may explain the unusual differences between the shallow and deep aftershocks.

The factors underlying energy dissipation during earthquake ruptures are generally not well understood. There is reason to believe that more efficient ruptures have higher rupture velocities, since more energy is available for rupture propagation (Kanamori & Rivera, 2006). An alternative way of stating this is that since less energy is dissipated near the crack tip, the fault zone width is narrower. Studies of particle size distributions and the gouge volume on the Punchbowl and San Andreas faults in Southern California suggest that ruptures on these faults dissipate very little energy, and that the slip zone itself is highly localized (Chester et al., 2005; Wilson et al., 2005). In contrast, the low radiation efficiency of the 2016 Tottori earthquake suggests that the slip zone was broader than that of more mature faults, and that about 95% of the available strain energy was dissipated as thermal and fracturing processes near the fault tip and the surrounding rock. The 2016 M_w 5.2 Borrego Springs and 2008 M_w 5.4 Chino Hills earthquakes in Southern California, for comparison, were estimated to have radiation efficiency values of 15–26% and 30%, respectively (Ross, Kanamori, & Hauksson, 2017; Shao et al., 2012). These earthquakes also occurred in geometrically complex fault zones, although the strain rate there is considerably larger than in the Tottori Prefecture. As these are only a small sample of events, more work is necessary to determine whether intraplate or geometrically complex regions are predisposed to producing ruptures that are highly inefficient.

Appendix A

Since a slip inversion involves many parameters and complex trade-offs between them, it is often difficult to determine which parameters are constrained well and which are not. Thus, an interpretation of the data using a simple directivity method helps to build intuition. In the case of the 2016 Tottori earthquake, it is reasonable to assume, from the fault geometry, that it can be approximated by a simple unilateral line source on a vertical plane. Using the simple unilateral Haskell model (Haskell, 1964), and denoting, the observed pulse width, rupture length, rupture velocity, phase speed, the azimuth of the station from the rupture direction, and the local rise time by T, L, V, c, θ, and τ, respectively,

$$T(\theta) = \frac{L}{V} - \frac{L}{c}\cos\theta + \tau. \tag{A1}$$

Then,

$$L = \frac{c}{2}[T(\pi) - T(0)], \tag{A2}$$

$$V = \frac{L}{\left[\frac{1}{2}(T(\pi) + T(0)) - \tau\right]}, \tag{A3}$$

and

$$T(\pi/2) = \frac{1}{2}[T(\pi) + T(0)]. \tag{A4}$$

The most important aspects of these equations are $T(0)$ and $T(\pi)$. From the deconvolved waveforms, if we use $T(0)$ = 2.0 s and $T(\pi)$ = 4.2 s and use c = 3.63 km/s, then from ((2)), we get L = 4.0 km. Then from ((3)), we get V = 1.90 km/s for τ = 1.0 s. Also, we get from ((4a))–((4c)), $T(\pi/2)$ = 3.1 s.

The actual data are more complex and suggest some secondary, probably scattered, patches on the fault plane, but these values approximately represent the main slip patch. Also, the rupture speed appears a little low, but this should apply to the initial patch. Other sets of ($T(0)$, $T(\pi)$, c, τ) may lead to minor variations around these values, but in general, the inversion results seem reasonable in light of this simple model.

Acknowledgments
The manuscript benefitted from constructive comments made by two anonymous reviewers. The authors are grateful to Doug Dreger and Ahyi Kim for their assistance with the Parkfield accelerograms and thank David Shelly for helpful discussions. The Hi-net, K-NET, KiK-net, and F-net data used in this study were provided by the National Research Institute for Earth Science and Disaster Prevention of Japan. The initial seismicity catalog was provided by the Japanese Meteorological Agency (JMA). The slip model and relocated seismicity catalog are provided in the supporting information. The Parkfield data are available from the Center for Engineering Strong Motion Data (strongmotioncenter.org). There are no real or perceived financial conflicts of interest for any author. The study was funded by the Gordon and Betty Moore Foundation, and NSF award EAR-1550704.

References

Allmann, B. P., & Shearer, P. M. (2007). Spatial and temporal stress drop variations in small earthquakes near Parkfield, California. *Journal of Geophysical Research*, *112*, B04305. https://doi.org/10.1029/2006JB004395

Andrews, D. J., & Ben-Zion, Y. (1997). Wrinkle-like slip pulse on a fault between different materials. *Journal of Geophysical Research*, *102*, 553–571. https://doi.org/10.1029/96JB02856

Aso, N., & Ide, S. (2014). Focal mechanisms of deep low-frequency earthquakes in eastern Shimane in western Japan. *Journal of Geophysical Research: Solid Earth*, *119*, 364–377. https://doi.org/10.1002/2013JB010681

Aso, N., Ohta, K., & Ide, S. (2013). Tectonic, volcanic, and semi-volcanic deep low-frequency earthquakes in western Japan. *Tectonophysics*, *600*, 27–40. https://doi.org/10.1016/j.tecto.2012.12.015

Aster, R. C., Borchers, B., & Thurber, C. H. (2012). *Parameter estimation and inverse problems*. Oxford, UK: Elsevier.

Ben-Zion, Y., & Ampuero, J.-P. (2009). Seismic radiation from regions sustaining material damage. *Geophysical Journal International*, *178*(3), 1351–1356. https://doi.org/10.1111/j.1365-246X.2009.04285.x

Ben-Zion, Y., & Sammis, C. G. (2003). Characterization of fault zones. *Pure and Applied Geophysics*, *160*(3), 677–715. https://doi.org/10.1007/pl00012554

Beroza, G. C. (1991). Near-source modeling of the Loma Prieta earthquake: Evidence for heterogeneous slip and implications for earthquake hazard. *Bulletin of the Seismological Society of America*, *81*(5), 1603–1621.

Beroza, G. C., & Spudich, P. (1988). Linearized inversion for fault rupture behavior: Application to the 1984 Morgan Hill, California, earthquake. *Journal of Geophysical Research*, *93*, 6275–6296. https://doi.org/10.1029/JB093iB06p06275

Brune, J. N. (1970). Tectonic stress and the spectra of seismic shear waves from earthquakes. *Journal of Geophysical Research*, *75*, 4997–5009. https://doi.org/10.1029/JB075i026p04997

Chester, J. S., Chester, F. M., & Kronenberg, A. K. (2005). Fracture surface energy of the Punchbowl fault, San Andreas system. *Nature*, *437*(7055), 133–136. https://doi.org/10.1038/nature03942

Duputel, Z., Rivera, L., Kanamori, H., & Hayes, G. (2012). W phase source inversion for moderate to large earthquakes (1990–2010). *Geophysical Journal International*, *189*(2), 1125–1147. https://doi.org/10.1111/j.1365-246X.2012.05419.x

Fukuyama, E., Ellsworth, W. L., Waldhauser, F., & Kubo, A. (2003). Detailed fault structure of the 2000 western Tottori, Japan, earthquake sequence. *Bulletin of the Seismological Society of America*, *93*(4), 1468–1478. https://doi.org/10.1785/0120020123

Gutscher, M. A., & Lallemand, S. E. (1999). Birth of a major strike-slip fault in SW Japan. *Terra Nova*, *11*(5), 203–209. https://doi.org/10.1046/j.1365-3121.1999.00247.x

Hartzell, S. H., & Heaton, T. H. (1983). Inversion of strong ground motion and teleseismic waveform data for the fault rupture history of the 1979 Imperial Valley, California, earthquake. *Bulletin of the Seismological Society of America*, *73*(6A), 1553–1583.

Haskell, N. A. (1964). Total energy and energy spectral density of elastic wave radiation from propagating faults. *Bulletin of the Seismological Society of America*, *54*(6A), 1811–1841.

Hauksson, E., Yang, W. Z., & Shearer, P. M. (2012). Waveform relocated earthquake catalog for Southern California (1981 to June 2011). *Bulletin of the Seismological Society of America*, *102*(5), 2239–2244. https://doi.org/10.1785/0120120010

Kagawa, T., Noguchi, T., Yoshida, S., & Yamamoto, S. (2017). Effect of the surface geology on strong ground motions due to the 2016 Central Tottori earthquake, Japan. *Earth, Planets and Space*, *69*(1), 106. https://doi.org/10.1186/s40623-017-0689-0

Kanamori, H. (1972). Determination of effective tectonic stress associated with earthquake faulting. The Tottori earthquake of 1943. *Physics of the Earth and Planetary Interiors*, *5*, 426–434. https://doi.org/10.1016/0031-9201(72)90114-8

Kanamori, H., & Rivera, L. (2006). Energy partitioning during an earthquake. In R. Abercrombie, A. McGarr, G. D. Toro, & H. Kanamori (Eds.), *Earthquakes: Radiated energy and the physics of faulting* (pp. 3–13). Washington, DC: American Geophysical Union. https://doi.org/10.1029/170GM03

Kanamori, H., & Rivera, L. (2008). Source inversion of W phase: Speeding up seismic tsunami warning. *Geophysical Journal International*, *175*(1), 222–238. https://doi.org/10.1111/j.1365-246X.2008.03887.x

Kaneda, H., & Okada, A. (2002). Surface rupture associated with the 1943 Tottori earthquake: Compilation of previous reports and its tectonic geomorphological implications. *Active Fault Research*, *21*, 73–91.

Kikuchi, M., & Kanamori, H. (1982). Inversion of complex body waves. *Bulletin of the Seismological Society of America*, *72*(2), 491–506.

Kim, A., & Dreger, D. S. (2008). Rupture process of the 2004 Parkfield earthquake from near-fault seismic waveform and geodetic records. *Journal of Geophysical Research*, *113*, B07308. https://doi.org/10.1029/2007JB005115

Kubo, H., Suzuki, W., Aoi, S., & Sekiguchi, H. (2017). Source rupture process of the 2016 central Tottori, Japan, earthquake (M JMA 6.6) inferred from strong motion waveforms. *Earth, Planets and Space*, *69*(1), 127. https://doi.org/10.1186/s40623-017-0714-3

Li, Y.-G., Chen, P., Cochran, E. S., Vidale, J. E., & Burdette, T. (2006). Seismic evidence for rock damage and healing on the San Andreas fault associated with the 2004 M 6.0 Parkfield earthquake. *Bulletin of the Seismological Society of America*, *96*(4B), S349–S363. https://doi.org/10.1785/0120050803

Ligorría, J. P., & Ammon, C. J. (1999). Iterative deconvolution and receiver-function estimation. *Bulletin of the Seismological Society of America*, *89*(5), 1395–1400.

Mendoza, C., & Hartzell, S. H. (1988). Aftershock patterns and main shock faulting. *Bulletin of the Seismological Society of America*, *78*(4), 1438–1449.

Nishida, R. (1990). Characteristics of the 1983 Tottori earthquake sequence and its relation to the tectonic stress field. *Tectonophysics*, *174*(3-4), 257–278. https://doi.org/10.1016/0040-1951(90)90325-3

Nishimura, T., & Takada, Y. (2017). San-in Shear Zone in southwest Japan, revealed by GNSS observations. *Earth, Planets and Space*, *69*(1), 85. https://doi.org/10.1186/s40623-017-0673-8

Noda, H., Lapusta, N., & Kanamori, H. (2013). Comparison of average stress drop measures for ruptures with heterogeneous stress change and implications for earthquake physics. *Geophysical Journal International*, *193*(3), 1691–1712. https://doi.org/10.1093/gji/ggt074

Ohmi, S., & Obara, K. (2002). Deep low-frequency earthquakes beneath the focal region of the M_w 6.7 2000 western Tottori earthquake. *Geophysical Research Letters*, *29*(16), 1807. https://doi.org/10.1029/2001GL014469

Okada, Y. (1985). Surface deformation due to shear and tensile faults in a half-space. *Bulletin of the Seismological Society of America*, *75*(4), 1135–1154.

Omote, S. (1943). The Tottori earthquake of March 4, 1943. *Bulletin of the Earthquake Research Institute-University of Tokyo*, *21*, 435–457.

Prieto, G. A., Parker, R. L., & Vernon, F. L. III (2009). A Fortran 90 library for multitaper spectrum analysis. *Computers & Geosciences*, *35*(8), 1701–1710. https://doi.org/10.1016/j.cageo.2008.06.007

Pulido, N., & Kubo, T. (2004). Near-fault strong motion complexity of the 2000 Tottori earthquake (Japan) from a broadband source asperity model. *Tectonophysics*, *390*(1-4), 177–192. https://doi.org/10.1016/j.tecto.2004.03.032

Ross, Z. E., White, M. C., Vernon, F. L., & Ben-Zion, Y. (2016). An improved algorithm for real-time *S*-wave picking with application to the (augmented) ANZA network in Southern California. *Bulletin of the Seismological Society of America.*, *106*(5), 2013–2022. https://doi.org/10.1785/0120150230

Ross, Z. E., Kanamori, H., & Hauksson, E. (2017). Anomalously large complete stress drop during the 2016 M_w 5.2 Borrego Springs earthquake inferred by waveform modeling and near-source aftershock deficit. *Geophysical Research Letters*, *44*, 5994–6001. https://doi.org/10.1002/2017GL073338

Ross, Z. E., Rollins, C., Cochran, E. S., Hauksson, E., Avouac, J.-P., & Ben-Zion, Y. (2017). Aftershocks driven by afterslip and fluid pressure sweeping through a fault-fracture mesh. *Geophysical Research Letters*, *44*, 8260–8267. https://doi.org/10.1002/2017GL074634

Semmane, F., Cotton, F., & Campillo, M. (2005). The 2000 Tottori earthquake: A shallow earthquake with no surface rupture and slip properties controlled by depth. *Journal of Geophysical Research*, *110*, B03306. https://doi.org/10.1029/2004JB003194

Shao, G., Ji, C., & Hauksson, E. (2012). Rupture process and energy budget of the 29 July 2008 M_w 5.4 Chino Hills, California, earthquake. *Journal of Geophysical Research*, *117*, B07307. https://doi.org/10.1029/2011JB008856

Shelly, D. R., Ellsworth, W. L., & Hill, D. P. (2016). Fluid-faulting evolution in high definition: Connecting fault structure and frequency-magnitude variations during the 2014 Long Valley caldera, California, earthquake swarm. *Journal of Geophysical Research: Solid Earth*, *121*, 1776–1795. https://doi.org/10.1002/2015jb012719

Shibutani, T., Nakao, S., Nishida, R., Takeuchi, F., Watanabe, K., & Umeda, Y. (2002). Swarm-Like seismic activity in 1989, 1990 and 1997 preceding the 2000 western Tottori earthquake. *Earth, Planets and Space*, *54*(8), 831–845. https://doi.org/10.1186/BF03352076

Shibutani, T., Katao, H., & Earthquake, G. of the 2000 W. T (2005). High resolution 3-D velocity structure in the source region of the 2000 western Tottori earthquake in southwestern Honshu, Japan using very dense aftershock observations. *Earth, Planets and Space*, *57*(9), 825–838. https://doi.org/10.1186/BF03351861

Shipton, Z. K., Evans, J. P., Abercrombie, R. E., & Brodsky, E. E. (2006). The missing sinks: Slip localization in faults, damage zones, and the seismic energy budget. In R. Abercrombie, A. McGarr, G. D. Toro, & H. Kanamori (Eds.), *Earthquakes: Radiated energy and the physics of faulting* (pp. 217–222). Washington, DC: American Geophysical Union. https://doi.org/10.1029/170GM22

Thomson, D. J. (1982). Spectrum estimation and harmonic analysis. *Proceedings of the IEEE*, *70*(9), 1055–1096. https://doi.org/10.1109/PROC.1982.12433

Trugman, D. T., & Shearer, P. M. (2017). A hierarchical clustering algorithm for relative earthquake relocation, With application to the Spanish Springs and Sheldon, Nevada, earthquake sequences. *Seismological Research Letters*, *88*(2A), 379–391. https://doi.org/10.1785/0220160188

Tsuya, H. (1944). Geological observations of earthquake faults of 1943 in Tottori Prefecture. *Tokyo Imperial University Earthquake Research Institute Bulletin*, *22*, 1–32.

Vassiliou, M., & Kanamori, H. (1982). The energy release in earthquakes. *Bulletin of the Seismological Society of America*, *72*(2), 371–387.

Weertman, J. (1980). Unstable slippage across a fault that separates elastic media of different elastic constants. *Journal of Geophysical Research*, *85*, 1455–1461. https://doi.org/10.1029/JB085iB03p01455

Wilson, B., Dewers, T., Reches, Z., & Brune, J. (2005). Particle size and energetics of gouge from earthquake rupture zones. *Nature*, *434*(7034), 749–752. https://doi.org/10.1038/nature03433

Xu, S., Ben-Zion, Y., Ampuero, J.-P., & Lyakhovsky, V. (2015). Dynamic ruptures on a frictional Interface with off-fault brittle damage: Feedback mechanisms and effects on slip and near-fault motion. *Pure and Applied Geophysics*, *172*(5), 1243–1267. https://doi.org/10.1007/s00024-014-0923-7

Ye, L., Lay, T., Kanamori, H., & Rivera, L. (2016). Rupture characteristics of major and great ($M_w \geq 7.0$) megathrust earthquakes from 1990 to 2015: 2. Depth dependence. *Journal of Geophysical Research: Solid Earth*, *121*, 845–863. https://doi.org/10.1002/2015JB012427